ACS APPLIED MATERIALS & INTERFACES

Article

Microfluidic Immuno-Biochip for Detection of Breast Cancer Biomarkers Using Hierarchical Composite of Porous Graphene and Titanium Dioxide Nanofibers

Md. Azahar Ali, Kunal Mondal, Yueyi Jiao, Seval Oren, Zhen Xu, Ashutosh Sharma, and Liang Dong

ACS Appl. Mater. Interfaces, **Just Accepted Manuscript** • DOI: 10.1021/acsami.6b05648 • Publication Date (Web): 21 Jul 2016

ACS Publications

ACS Applied Materials & Interfaces is published by the American Chemical Society.
1155 Sixteenth Street N.W., Washington, DC 20036

Microfluidic Immuno-Biochip for Detection of Breast Cancer Biomarkers Using Hierarchical Composite of Porous Graphene and Titanium Dioxide Nanofibers

Md. Azahar Ali[a], Kunal Mondal[b], Yueyi Jiao[a], Seval Oren[a], Zhen Xu[a], Ashutosh Sharma[c], and Liang Dong[a,*]

[a]Department of Electrical and Computer Engineering, Iowa State University, Ames, IA 50011, USA
[b]Department of Chemical and Biomolecular Engineering, North Carolina State University, Raleigh, NC 27695, USA
[c]Department of Chemical Engineering, Indian Institute of Technology Kanpur, Kanpur 208016, India

ABSTRACT

We report on a label-free microfluidic immunosensor with femtomolar sensitivity and high selectivity for early detection of epidermal growth factor receptor 2 (*EGFR2* or *ErbB2*) proteins. This sensor utilizes a uniquely structured immunoelectrode made of porous hierarchical graphene foam (GF) modified with electrospun carbon-doped titanium dioxide nanofibers ($nTiO_2$) as an electrochemical working electrode. Due to excellent biocompatibility, intrinsic surface defects, high reaction kinetics, and good stability for proteins, anatase $nTiO_2$ are ideal for electrochemical sensor applications. The three-dimensional and porous features of GF allow $nTiO_2$ to penetrate and attach to the surface of the GF by physical adsorption. Combining GF with functional $nTiO_2$ yields high charge transfer resistance, large surface area, and porous access to the sensing surface by the analyte, resulting in new possibilities for the development of electrochemical immunosensors. Here, the enabling of EDC–NHS chemistry covalently immobilized the antibody of *ErbB2* (anti-*ErbB2*) on the GF–$nTiO_2$ composite. To obtain a compact sensor architecture, the composite working electrode was designed to hang above the gold counter electrode in a microfluidic channel. The sensor underwent differential pulse voltammetry and electrochemical impedance spectroscopy to quantify breast cancer biomarkers. The two methods had high sensitivities of 0.585 $\mu A\ \mu M^{-1}\ cm^{-2}$ and 43.7 $k\Omega\ \mu M^{-1}\ cm^{-2}$ in a wide concentration range of target ErbB2 antigen from 1×10^{-15} M (1.0 fM) to 0.1×10^{-6} M (0.1 μM), and from 1×10^{-13} M (0.1 pM) to 0.1×10^{-6} M (0.1 μM), respectively. Utilization of the specific recognition element (i.e., anti-*ErbB2*) results in high specificity, even in the presence of identical members of the *EGFR* family of receptor tyrosine kinases, such as ErbB3 and ErbB4. Many promising applications in the field of electrochemical detection of chemical and biological species will derive from the integration of the porous GF–$nTiO_2$ composite into microfluidic devices.

Keywords: Cancer immunodiagnostics, Microfluidics, Carbon-doped titanium dioxide, Graphene foam, Biosensor, Electrochemical detection

1. INTRODUCTION

Point-of-care detection devices are highly desirable for early diagnosis of diseases, but they require high sensitivity and specificity with minimum sample consumption and must be easy to operate.[1,2] The quantification of protein biomarkers for the diagnosis and prognosis of breast cancer, inflammation, and bacterial, viral, and neurodegenerative diseases has received some attention recently.[3] In particular, the detection of breast cancer biomarkers at an early stage is extremely important for clinical diagnosis and treatment and thus for patient survival.[4] There are four members of the human epidermal growth factor receptor (*ErbB*) family: *ErbB1*, *ErbB2*, *ErbB3*, and *ErbB4*.[5] *ErbB2* (also known as EGFR2 and HER2) is considered a noninvasive tool for early breast cancer diagnosis.[6,7] The *ErbB2* gene belongs to the mammalian *EGFR* family and encodes a 185-kDa transmembrane glycoprotein and a receptor tyrosine kinase with intrinsic tyrosine kinase activity.[8] Receptor tyrosine kinases have a strong affinity to cell surface receptors. Overexpression (~30%) of several receptor tyrosine kinases in *ErbB2* is associated with increasing breast cancer metastasis.[6,9] The excessive signaling of *ErbB2* is a critical factor in the development of malignant cancerous tumors and also can cause other cancers such as ovarian, bladder, salivary, stomach, and lung carcinomas.[10] Several methods, including X-ray mammography, magnetic resonance imaging, computed tomography, and ultrasound imaging, are commonly used to monitor cancerous tumors.[11] However, these technologies rely heavily on imaging to determine tumor status and thus provide limited information about the onset of cancer and limited monitoring of early-stage cancerous cells. Other methods for cancer detection, such as enzyme-linked immunoabsorbent assay (ELISA),[12] immunoblotting, and immunohistochemistry,[13] require complex purification and pretreatment processes, or are used as semi quantitative methods. The limits of state-of-art commercial immunoassays, such as

Abbott IMX,[14] Roche Elecsys,[15] and Hybritech Tandem R,[16] for detecting various proteins in 50–150 µL sample volumes are in the 10–100 pg/mL range.[17]

Recently, many new technologies, such as surface plasmon resonance,[18] photonic crystals,[19] microcantilevers,[20] semiconductor quantum dots,[21] and nanotransistors,[17] have demonstrated their remarkable enhanced ability to quantify breast cancer biomarkers. Ho et al.[22] reported the use of an immune magnetic platform for multiplex quantification of cancer-associated proteins such as alpha-fetoprotein, carcinoembryonic antigen, and prostate-specific antigen (PSA). The use of graphene-encapsulated nanoparticles helped realize a sensitive field-effect transistor-based immunosensor for quantifying breast cancer biomarkers with a detection limit of 1×10^{-12} M (1.0 pM).[23] Mani et al.[24] demonstrated an electrochemical immunosensor that uses densely packed gold nanoparticles combined with multiple-enzyme-labeled antibody magnetic beads to detect the cancer biomarker PSA. Yu et al.[17] showed that the combination of immunosensors with single-wall carbon nanotubes and multilabel secondary antibodies detects cancer biomarkers with good sensitivity. Wang et al.[25] reported on a magnetically induced solid-state electrochemical platform capable of detecting breast cancer biomarkers at a detection limit of 200 ng mL^{-1} via DNA hybridization. Gao et al.[26] reported on impedimetric detection of cancerous molecules using carbon nanotubes, modified with gold nanoparticles, as an electrochemical electrode for immobilizing anti-carcinoembryonic antigen, resulting in a detection limit of 0.06 ng mL^{-1} in a range of 0.1–160 ng mL^{-1}.

Functional graphene has received considerable attention because of its large surface area, superior electroactivity, ease of functionalization with antibodies and other bioreceptors, and high mechanical strength.[27,28] In addition, because of its excellent electrical conductivity, graphene can act as an “electron wire” whereby it establishes a conduction path for rapid electron transfer for selective detection of target species.[28,29] Recently, three-dimensional (3D)

hierarchical porous graphene foam (GF) capable of rapidly transferring electrons along the continuously interconnected graphene building blocks was realized via a template-directed chemical vapor deposition method.[30,31] Its large surface area (up to ~850 $m^2 g^{-1}$) and porosity make GF suitable for integration with nanostructured materials without agglomeration.[32] With a pore diameter of 50–250 μm, GF is an ideal scaffold for the fabrication of monolithic composite electrodes. Nanostructure-based GF composites have been used in devices such as supercapacitors,[33] field emitters, and photocatalysts.[34] Deposition of vertically aligned ZnO nanowires on GF has resulted in the detection of uric acid, dopamine, and ascorbic acid with nanomolar sensitivity.[35] Co_3O_4[32] and Mn_3O_4[36] nanostructures also have been grown in GF for electrochemical glucose biosensors with high sensitivity and improved detection limit. Thus, the synergistic effect from the integration of nanostructures with GF has shown that there is great potential for the improvement of biosensing efficacy.

Recently, highly sensitive chemical and biological sensors[37, 38,39] have become possible because of nanostructured metal oxide materials, particularly those in the form of one-dimensional (1D) fiber or wire. Their reduced size, high aspect ratio, dimensions comparable to the Debye length, and fast transfer of electrons resulting from molecular recognition events along the entire fiber make these materials good candidates for sensors.[38,40] In addition, oxygen vacancy-induced point defects in TiO_2 are within the bridging oxygen rows of the (110)−(1 × 1) surface, resulting in the potential to be stabilized with adsorbates on the surface.[41] TiO_2 nanofibers ($nTiO_2$) have excellent charge transfer resistance, insignificant protein denaturation, high structural uniformity, long-term chemical stability, and biocompatibility.[38,39,42] Thus, a TiO_2 nanowire-based immunosensor has been developed to rapidly detect *Listeria monocytogenes* with high sensitivity.[43]

In this paper, we report on a microfluidic electrochemical sensor for the detection and immunodiagnosis of breast cancer biomarkers via antigen–antibody interactions. *The* sensor contains a unique 3D immunoelectrode consisting of a T-shaped porous GF structure modified with carbon-doped $nTiO_2$ and anti-*ErbB2* molecules. This immunoelectrode, the working electrode of the sensor, is hung from the upper side of a microfluidic channel, above the counter electrode positioned on the bottom of the channel (Fig. 1). The GF–$nTiO_2$ composite-based electrode integrated in the microfluidic device has a large specific surface area, 3D conductive pathways, and porous structure and provides remarkable detection of breast cancer biomarkers. In general, direct immobilization of biomolecules on the $nTiO_2$ surface via physical adsorption due to the low isoelectric points of $nTiO_2$ (~5.5; negatively charged) and anti-*ErbB2* (~5.8; negatively charged) is a major limitation.[38, 44] The carbon contents available in the GF– $nTiO_2$ composite allow for covalent binding with antibody molecules via the EDC–NHS coupling mechanism.[38] The amidation coupling reactions can cause the formation of amide bonds between the antibody and the GF–$nTiO_2$ matrix, resulting in an immunosensor with high stability and enhanced loading capacity for anti-*ErbB2*. In general, microscale sensors can provide superior performance compared with their large-scale counterparts. A miniaturized microfluidic device often allows for reduced consumption of agent and reagent, fast detection, well controlled microenvironment, and high portability. In addition, microfluidic integration with various sensing mechanisms may provide compact platforms for multiplexed detection of biological analytes from complex mixtures to realize high throughput assays. Specifically, the integration of the T-shaped porous immunoelectrode into a microfluidic channel and other microelectrodes results in a miniaturized sensor that requires reduced volumes of target fluids and chemical reagents. The porous nature of the immunoelectrode provides necessary

microscale passages for efficient handling of solutions during functionalization and detection inside a microfluidic channel.

To detect interfacial changes originating from biorecognition events at the proposed working electrode, we used electrochemical impedance spectroscopy (EIS) and differential pulse voltammetry (DPV) with this microfluidic sensor. The incorporation of the semiconductor $nTiO_2$ into the porous GF improves the impedance signal in the EIS method for detecting the *ErbB2* antigen. On the other hand, the low conductivity of $nTiO_2$ yields an inadequate response for DPV. Thus, a coating of $nTiO_2$ on highly conductive GF scaffolds can obviate this problem. Our microfluidic immunosensor with the unique GF–$nTiO_2$ structure is able to detect *ErbB2* in a wide concentration range (1.0 fM to 0.1 µM) and provides high stability, reproducibility, and selectivity, even in the presence of nonspecific antigen molecules such as *ErbB3* and *ErbB4*.

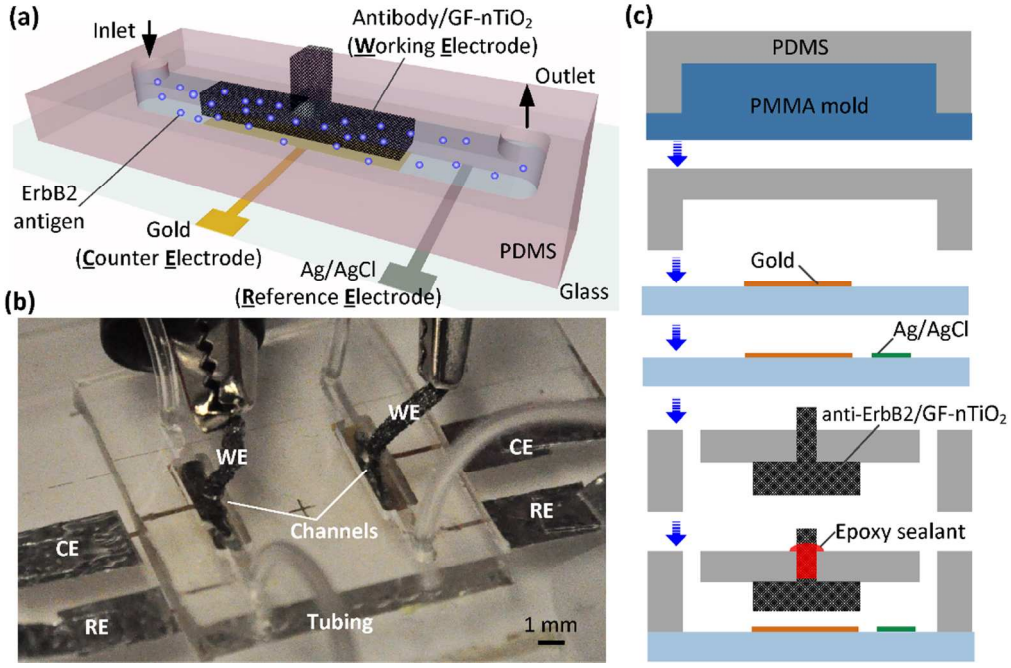

Fig. 1 (a) Schematic of the microfluidic immunosensor with 3D porous GF electrode modified with carbon-doped TiO_2 nanofibers for the detection of breast cancer biomarkers. (b) Photo of two microfluidic immunosensors. (c) Schematic representation of the fabrication of the microfluidic sensor.

2. EXPERIMENTAL SECTION

2.1 Chemicals. The 3D multilayer GF (99% carbon content; thickness = 1.2 mm; density = 4.0 mg/cm^3; pore size = 580 μm) was purchased from Graphene-Supermarket (Graphene Laboratories, Calverton, NY, USA). Titanium (IV) isopropoxide (MW = 284.2 g/mol) and polyvinylpyrrolidone (PVP) (MW = 1,300,000 g/mol) were obtained from Sigma-Aldrich (St. Louis, MO, USA). Absolute ethanol and glacial acetic acid (99.8%) were purchased from Merck (Kenilworth, NJ, USA) and Fischer Scientific (Waltham, MA, USA), respectively. *N*-Hydroxysuccinimide (NHS) and *N*-ethyl-N_0-(3-dimethylaminopropyl)carbodiimide (EDC) were purchased from Sigma−Aldrich. Lyophilized powder of human CellExp™ *ErbB2* (fused with polyhistidine tag at the C-terminus; MW = 72.4 kDa; source: HEK293 cells), *ErbB3* (MW = 71.5 kDa), and ErbB4 (fused with 6×histidine tag at the C-terminus, MW = 70.6 kDa) and human recombinant were purchased from BioVision (Milpitas, CA, USA). The stock solutions of *ErbB2*, *ErbB3*, and *ErbB4* were prepared with phosphate-buffered saline (PBS; pH 7.4) and diluted from 0.1 μM to 1.0 fM concentration. Rabbit polyclonal antibody of *ErbB2* (anti-*ErbB2*), soluble in PBS of pH 7.4 containing 30% glycerol, 1% bovine serum albumin (BSA), and 0.02% thimerosal, was purchased from BioVision. Polydimethylsiloxane (PDMS, Sylgard 184 kit) was obtained from Dow Corning (Midland, MI, USA). Deionized (DI) water (resistivity = 18.2 MΩ cm) (Millipore, Billerica, MA, USA) was used in all experiments. All chemicals were analytical grade and used as received without any purification.

2.2 Synthesis of carbon-doped nTiO_2. The electrospinning technique was used to form nTiO_2, for which titanium isopropoxide [Ti(O*i*Pr)$_4$] was the sol-gel precursor material. This improved process has been described previously.[45,46] In brief, 1.8 g of PVP was mixed with 30 mL of ethanol and stirred for 5–7 min. Separately, 6 g of Ti(O*i*Pr)$_4$ was added to a 24 mL solution of glacial acetic acid and ethanol, with a volume ratio of 1:1. The mixture was stirred and then mixed with the PVP solution. Then, 60 mL of this combined solution was magnetically stirred for 3.5 h and immediately loaded into a plastic medical syringe with a 26-gauge metallic needle. The needle was attached to a high-voltage DC power supply

(Gamma High Voltage, Ormond Beach, FL, USA) that could produce voltages up to 30 kV. The solution feeding rate was controlled by a syringe pump (Harvard Apparatus, Holliston, MA, USA). Fiber spinning began upon immediate application of voltage. The fibers were electrospun on a rotating cylindrical electrode that was covered with aluminum foil and positioned horizontally ~5–7 cm from the needle tip. The electrospun Ti(O*i*Pr)$_4$/PVP polymeric composite nanofibers were then collected and stabilized overnight in an air oven at 50 ^{o}C. Finally, the fibers were placed in a furnace with a 2 ^{o}C/min ramp rate and subjected to *controlled* calcination at 400 ^{o}C for 3 h to selectively eliminate the PVP component from the nTiO_2.

The controlled synthesis of carbon-doped nTiO_2 has been previously discussed.[46] To dope the synthesized nTiO_2 with carbon, the electrospun Ti(O*i*Pr)$_4$/PVP polymeric nanofibers were heat-treated at 350–400 °C for 2.5 h in the presence of air. The heat treatment converted the Ti(O*i*Pr)$_4$/PVP polymeric composite nanofibers into pure anatase nTiO_2. The selective removal of PVP by the controlled heating produced residual carbon, which acts as the dopant, the amount of which was optimized via the calcination process. Raman studies have confirmed the existence of amorphous carbon in nTiO_2 owing to inadequate removal of the polymer (Fig. S1, Supporting Information). In Raman spectra, the appearance of 1353 and 1598 cm^{-1} peaks in carbon-doped nTiO_2 indicates D and G bands, respectively.[47] Raman spectra also confirm the presence of anatase nTiO_2 and four robust peaks at 139.5, 392, 511, and 632 cm^{-1}. The peaks at 139.5 and 632 cm^{-1} correspond to the E_g mode of phonon vibration, while the peaks at 392 and 511 cm^{-1} correspond to the B_{1g} and A_{1g} modes, respectively. These peaks are indicative of the existence of the anatase phase in nTiO_2.

2.3 Instruments. The morphologies of the synthesized nTiO_2, GF, and GF–nTiO_2 composite were characterized using scanning electron microscopy (SEM, Supra 400VP, Zeiss, Oberkochen, Germany). The morphology of the nTiO_2 was further characterized using transmission electron microscopy (TEM, Tecnai

G2, FEI, Hillsboro, OR, USA). X-ray photoelectron spectroscopy (XPS) measurements were performed on $nTiO_2$, GF, GF–$nTiO_2$, and anti-*ErbB2*/GF–$nTiO_2$ samples using an Amicus/ESCA 3400 instrument (Kratos, Manchester, UK). These samples were irradiated with 240 W unmonochromatized Mg *Kα* X-rays, and the energy of the photoelectrons emitted at 0° normal to the surface was analyzed using a DuPont analyzer (DuPont, Wilmington, DE, USA). The pass energy was set at 75 eV and a Shirley baseline was subtracted from all reported spectra; CasaXPS was used to process the raw data files. A Zive Potentiostat SP1 (eDAQ, Colorado Springs, CO, USA) measured EIS and DPV in PBS (pH 7.4) containing 5 mM of both $[Fe(CN)_6]^{3-}$ and $[Fe(CN)_6]^{4-}$. The counter and reference electrodes were Au and Ag/AgCl, respectively.

2.4 Device Fabrication. Soft lithography was used to fabricate a PDMS channel (10 mm long, 1.5 mm wide, and 1.5 mm deep) (Fig. 1c). The channel pattern was designed by AutoCAD software (Autodesk, San Rafael, CA, USA) and then a master mold was formed in a poly(methyl methacrylate) (PMMA) slab using a high-precision milling machine (CNC Masters, Irwindale, CA, USA). Two-parts cure PDMS precursor solution (A:B weighing ratio = 10:1) was mixed and then degassed in a homemade chamber for 30 min under vacuum (10^{-4} Torr). The degassed PDMS solution was then poured over the master mold in a disposable polystyrene petri dish (diameter = 100 mm; Sigma-Aldrich) and baked on a hot plate at 80 ºC for 2 h. After heat curing, the PDMS channel device was peeled off the master mold. The channel was utilized to direct various solutions to the sensing area and further to the waste reservoir external to the device. Meanwhile, a Au counter electrode and a Ag/AgCl reference electrode were fabricated on a glass slide (50 mm × 75 mm; thickness = 0.9 mm; Dow Corning). In this step, an 80-nm-thick Au thin film was deposited on a glass slide by e-beam evaporation and then patterned by conventional photolithography using a photoresist (AZ 5214 E). The photoresist was exposed for 20 s to ultraviolet light (intensity = 8 mW/cm^2) through a photomask that was printed on transparent film (3600 dpi) by a high-resolution plotter (Fineline Imaging, Colorado Springs, CO, USA). The patterned photoresist was baked on a hot plate at 90 ºC for 3 min. The wafer was then immersed in AZ photoresist

developer solution (Microchem, Westborough, MA, USA) for 2 min. Next, the Au thin film was selectively etched using Au etchant (GE-8148) and the photoresist was stripped off with acetone. The wafer was washed off with DI water and then air-dried. The Ag electrode was formed using the same fabrication procedure as that for the Au electrode, except for the deposition of a 700-nm-thick Ag film onto the glass slide containing the fabricated Au electrode and etching with Ag etchant (Silver Etchant TFS). The final product was treated with KCl (0.1 M) for 2 min to obtain the Ag/AgCl electrode.

The T-shaped GF electrode was modified with $nTiO_2$ and functionalized with anti-*ErbB2*. $nTiO_2$ powder (4 mg) was dispersed in 2 mL of pure ethanol and the solution was sonicated for 1 h at 25 ºC. Fifty microliters of the solution was then spread onto the surface of the GF electrode. Due to the high porosity of GF, the $nTiO_2$ suspension easily penetrated the GF electrode. The $nTiO_2$ attached onto the surface of the GF scaffold through physical adsorption. The modification of the GF with $nTiO_2$ increased the total surface area of the GF, thus increasing the ability to load antibodies and potentially increase the electrochemical output signals. Before immobilization of anti-*ErbB2*, the GF–$nTiO_2$ electrode was treated with oxygen plasma for 15 s to oxidize carbon and create carboxyl (–COOH) groups on its surface. These –COOH groups were then activated by EDC–NHS coupling. EDC is a crosslinking agent used to couple the –COOH groups on the GF–$nTiO_2$ surface to primary amines of anti-*ErbB2* ($–NH_2$), and NHS is an activator used to increase the stability of the active esters formed during the coupling reactions. For EDC–NHS coupling, 10 µL of EDC (0.2 M) solution was mixed with 10 µL of NHS (0.05 M) and spread onto the surface of the GF–$nTiO_2$ electrode. The electrode was kept in a humidity chamber (100% relative humidity) for 4 h and then was washed with PBS. Subsequently, 20 µL of anti-*ErbB2* solution (0.24 µM) was spread on the surface of the GF–$nTiO_2$ electrode by drop casting. Again, the electrode was kept in a humidity chamber at 4 °C for 4 h and then was washed with PBS (pH 7.4).

Fig. 2 is a schematic of the functionalization of anti-*ErbB2* molecules on the surface of both the GF and the GF–$nTiO_2$. The –NH_2 amine groups of the anti-*ErbB2* were bound covalently with the –COOH groups from the GF and GF-$nTiO_2$ by forming C–N amide bonds. The nonspecific sites of anti-*ErbB2*/GF–$nTiO_2$ were blocked by treatment with BSA (2 mg/mL). Thus, the T-shaped BSA/anti-*ErbB2*/GF–$nTiO_2$ immunoelectrode was formed.

To attach the anti-*ErbB2*/GF–$nTiO_2$ immunoelectrode (WE) to the top of the PDMS channel, we punched a hole through the top PDMS layer and inserted the upside-down T-shaped immunoelectrode into the hole so that the horizontal part was inside the channel and the vertical part was above the PDMS channel for external electrical connections (see Fig. 1a). Next, a drop of degassed PDMS precursor solution was placed carefully in the hole and cured at room temperature. Oxygen plasma treatment permanently bonded the glass substrate containing the counter (CE) and reference (RE) electrodes and the PDMS slab containing the immunoelectrode. Thus, the WE hung from the top PDMS layer was parallel to the Au CE and ~300 μm apart. The parallel layout of the WE and CE inside the microfluidic channel reduces the size of the device and may also provide fast transport of electrons[48] due to redox reactions toward the WE resulting in increased electrochemical signals.

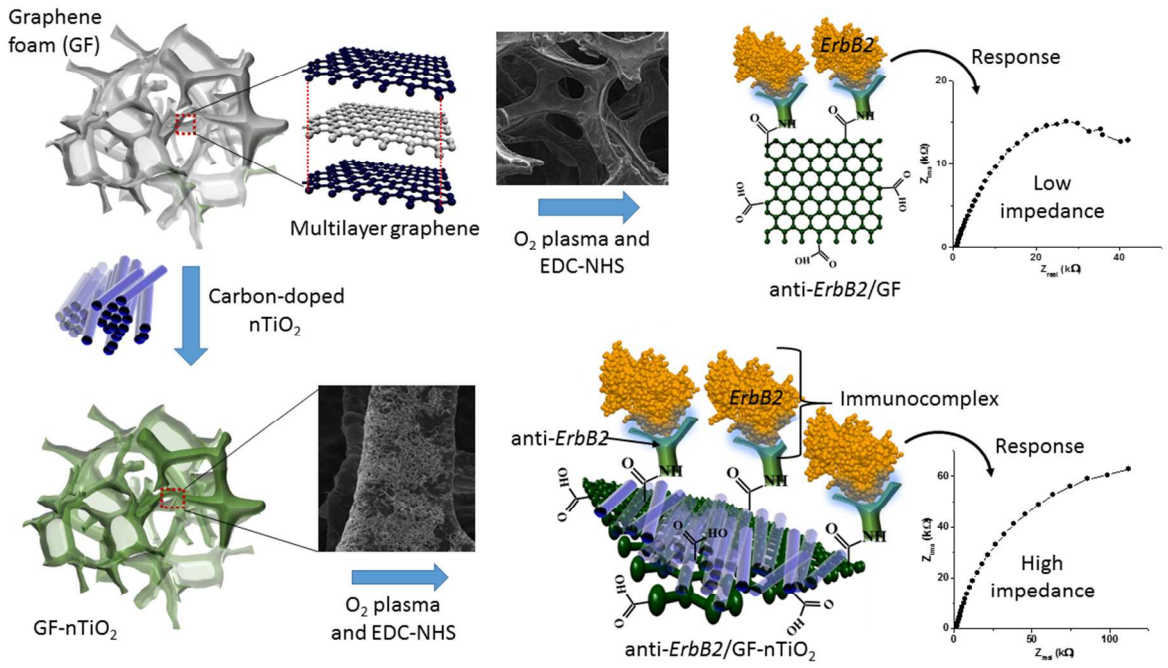

Fig. 2 Functionalization of anti-*ErbB2* molecules on the surface of GF and GF–nTiO_2 electrodes using EDC–NHS chemistry followed by oxygen plasma treatment.

3. RESULTS AND DISCUSSION

3.1 Microscopic Analyses. Field emission SEM (FESEM) imaging was used to study the surface morphologies of the nTiO_2, GF, and GF–nTiO_2 composite. Fig. 3a shows the solid, rod-like nTiO_2, which have an average diameter of 72 nm and are a few microns long. The TEM image in Fig. 3b shows that each nanofiber comprises a number of TiO_2 grains. The pore size of the GF ranges from 500 to 600 µm (Figs. 3c), which is large enough for the nanofibers to penetrate (Fig. 3d). Figs. 3d–3f show that the GF scaffold is almost entirely covered by randomly oriented nTiO_2. This coating increases the ability of the immunoelectrode to load antibodies via covalent interactions.

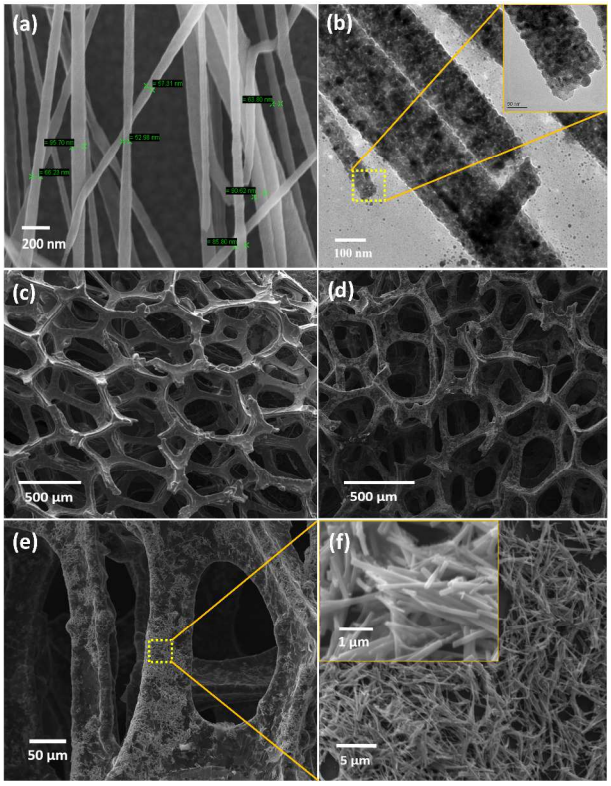

Fig. 3 (a) FESEM images of synthesized carbon-doped $nTiO_2$. (b) TEM image of carbon-doped $nTiO_2$. Inset shows a magnified image of a single $nTiO_2$. (c) SEM image of 3D GF. (d–f) SEM images of GF–$nTiO_2$ composite. The inset in (f) is a magnified image of the composite.

3.2 Spectroscopic Studies. XPS was used to confirm the presence of the functional groups in the carbon-doped $nTiO_2$, GF, and GF–$nTiO_2$, and the formation of amide between antibodies and GF–$nTiO_2$. The C 1s, O 1s, and Ti 2p peaks in the wide-scan spectrum of $nTiO_2$ indicate the formation of carbon dopant in $nTiO_2$ (Fig. S2a, Supporting Information). The O peak at 532 eV is from the formation of the Ti–O bond. The core-level spectra of C 1s were deconvoluted into characteristic peaks using a Shirley baseline with a Gaussian profile (Fig. S2b). The $nTiO_2$ peaks at 284.6, 287.0, and 288.9 eV correspond to the C–C neutral bond and oxidized C species such as C–O and –COOH, respectively.[49] The presence of these peaks may be due to the formation of carbonate-like species by interstitial carbon in the $nTiO_2$ lattice. The wide-scan spectra of GF showed the C 1s and O 1s peaks, and after coating the GF–$nTiO_2$ composite with anti-*ErbB2*, the N 1s peak appeared (Fig. S3a). The core-level spectra of the GF–$nTiO_2$ composite had a Ni 2p

peak at 852–858 eV as a result of the use of Ni template during the synthesis of GF (Fig. S3b). The peaks at 852.3and 856.9 eV are due to Ni $2p_{1/2}$ and Ni $2p_{3/2}$ in the GF–$nTiO_2$ composite. The Ti 2p peak was deconvoluted into characteristic peaks (Fig. S3c). The Ti $2p_{1/2}$ and Ti $2p_{3/2}$ peaks for $nTiO_2$ due to spin-orbit splitting photoelectrons were located at 465.4 and 459.4 eV, respectively, indicating the existence of Ti^{4+} ions (higher oxidation state) in $nTiO_2$.[49]

The XPS C 1s peaks at 284.3 and 285.2 eV for the GF electrode alone, without $nTiO_2$ and anti-*ErbB2*, correspond to the core-level spectra of carbon due to the graphitic nature of sp^2 (C–C) and a defect (sp^3, C=O), respectively (Fig. 4a, bottom graph).[50] After the GF surface was modified with $nTiO_2$, an additional peak occurred for C 1s at 288.9 eV, indicating the presence of O–C=O groups wherein the atomic ratio of the peak due to C=O is reduced 6.7% (Table S1, Supporting Information). After the functionalization of the antibodies on the oxygen plasma-treated GF–$nTiO_2$ by EDC–NHS chemistry, the binding energy of the C–O peak shifted by 1.1 eV and there were two additional peaks, at 287.1 and 290.0 eV, corresponding to N–C=O and carboxylic groups (O–C=O), respectively. The formation of an amide bond (N–C=O) is the result of the covalent interactions between –COOH groups on GF–$nTiO_2$ and $–NH_2$ groups on anti-*ErbB2*. Table 1 presents the % relative atomic concentration, the full width at half-maximum (FWHM), and the peak position of the deconvoluted C 1s, O 1s, and N 1s peaks in electrodes of various compositions. The O 1s peaks at 532.6 and 532.1 eV correspond to C–O and C=O, respectively, indicating the presence of defects in GF. With antibody loading, these peaks shifted to higher binding energies. Fig. 4c shows the N 1s core-level spectra for GF-$nTiO_2$ with and without anti-*ErbB2*. In addition, there were no peaks for electrons of N 1s in the GF–$nTiO_2$ composite alone. The three peaks at the binding energies of 398.3, 401.3, and 402.7 eV for the anti-*ErbB2*/GF–$nTiO_2$ are assigned to the core-level electron of N 1s, the amide N (CO–NH) present in the antibody/matrix, and the ≡N species, respectively.[50] This result indicates the successful functionalization of anti-*ErbB2* molecules on the surface of the GF–$nTiO_2$ electrode.

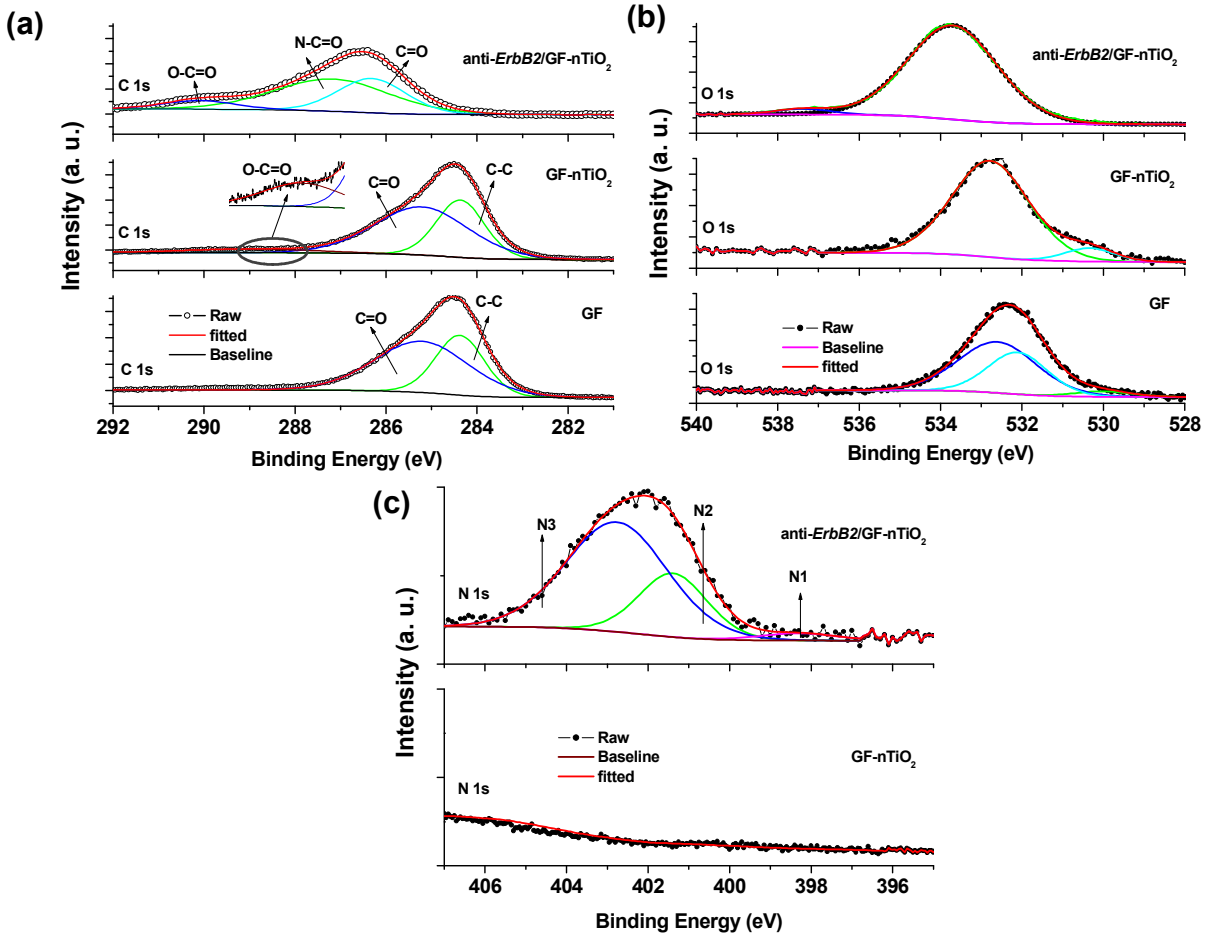

Fig. 4 XPS core-level spectra of (a) C 1s, (b) O 1s, and (c) N 1s for the GF, the GF–$nTiO_2$, and the anti-*ErbB2*/GF–$nTiO_2$ electrodes.

3.3 Electrochemical Characterization. The fabricated electrodes within their corresponding devices underwent EIS as a function of frequency (1.0 to 100 × 10^3 Hz) to investigate properties, such as charge transfer resistance (R_{ct}) and double-layer capacitance (C_{dl}), at the interface between the electrode and the electrolyte solution. Fig. 5a shows the Nyquist plots obtained by EIS, and the inset shows that R_{ct} is parallel to C_{dl} in the equivalent circuit model of the device. In the Nyquist plot of each electrode, the diameter of the semicircle (inset, Fig. 5a) represents the value of R_{ct} at high frequencies and implies a charge-transfer-limited behavior. The values of R_{ct} and C_{dl} can be obtained from the real ($\boldsymbol{Z}'$) and imaginary ($-\boldsymbol{Z}''$) components of complex impedance at different frequencies for a parallel RC circuit using Eq. (1):[51]

$$Z(\omega) = R_s + \frac{R_{ct}}{1+j\omega R_{ct}C_{dl}} = R_s + \frac{R_{ct}}{1+\omega^2 R_{ct}^2 C_{dl}^2} - \frac{j\omega R_{ct}^2 C_{dl}}{1+\omega^2 R_{ct}^2 C_{dl}^2} = Z' + jZ'' \quad (1)$$

The frequency associated with the maximum Z'', f_{max}, and the time constant τ can be calculated using Eq. (2):

$$R_{ct}C_{dl} = \frac{1}{2\pi f_{max}} = \tau \quad (2)$$

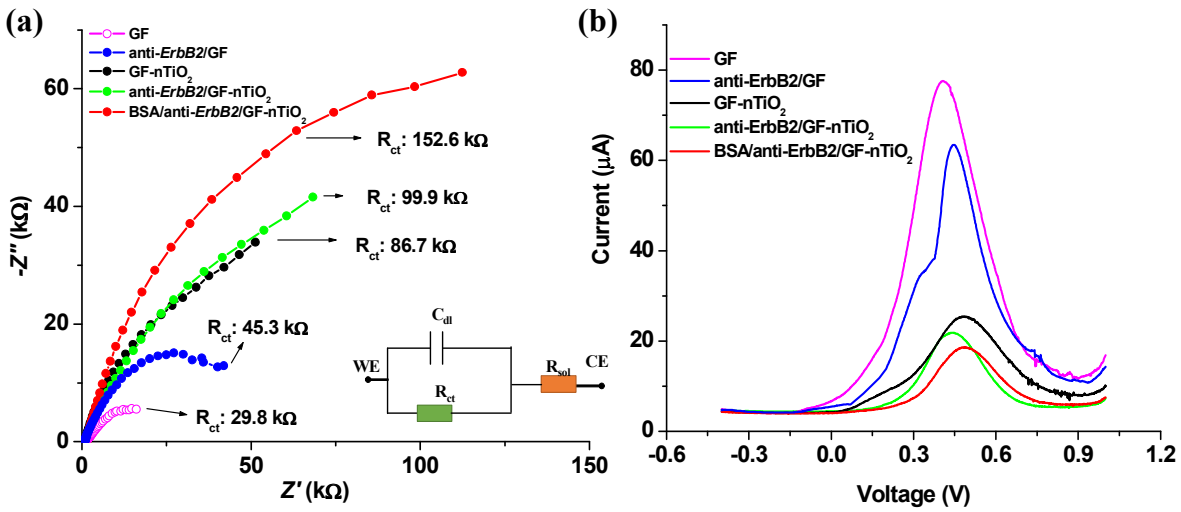

Fig. 5 (a) Nyquist plots for various fabricated electrodes embedded in the microfluidic device. Inset shows the equivalent circuit model for the Nyquist plot used to obtain the R_{ct} value. In EIS, the amplitude was set to 1 mV for a sinusoidal signal, the bias potential was set to 1 mV, and the frequency range was from 1.0 to 100×10^3 Hz. (b) DPV of the fabricated electrodes. Both the EIS and the DPV measurements were conducted in the presence of PBS (pH: 7.4) containing equimolar of 5 mM for both $[Fe(CN)_6]^{3-}$ and $[Fe(CN)_6]^{4-}$ as redox probes.

The GF-based device had an R_{ct} of 29.8 kΩ. However, after modification of GF with anti-*ErbB2*, the increase in R_{ct} to 45.3 kΩ was due to the formation of functional groups (e.g., –COOH, C–N, C=O) on the GF via plasma oxidation and EDC–NHS treatment, as evidenced by XPS (Fig. 4), as well as to the insulating nature of *ErbB2* antibodies at the GF which hinders electron transfer. Interestingly, the carbon-doped $nTiO_2$ coating on the GF scaffolds enhanced the value of R_{ct} by nearly three orders of magnitude (87.7 kΩ) because of the semiconducting properties of the oxygenated $nTiO_2$ compared to those of the GF alone. The porous GF provides easy access for

$nTiO_2$ to reach the interior scaffolds, thus enhancing the loading capacity of the GF for anti-*ErbB2*. After immobilization of the immunoelectrode with BSA proteins, R_{ct} increased to 152.6 kΩ because of the insulation provided by the proteins, which obstructed the redox conversion of $[Fe(CN)_6]^{3-/4-}$. The heterogeneous electron transfer (HET) rate constant (k_s) for all the electrodes is defined as[51]

$$k_s = RT/n^2F^2AR_{ct}C \quad (3)$$

where R is the gas constant (8.314 J/K mol), T is the temperature (298 K), n is the electron transfer constant of the redox couple (i.e., 1), F is Faraday's constant (96485.3 s A/mol), A is the area of the electrode (0.096 cm^2), and C is the concentration of the redox couple (5 mM) in the surrounding solution. k_s of the GF electrode was higher (18.6×10^{-6} cm s^{-1}) than those of the anti-*ErbB2*-immobilized GF and the $nTiO_2$-modified GF (Table 1). BSA and anti-*ErbB2* loaded onto the GF–$nTiO_2$ electrode further reduced k_s to 3.6×10^{-6} cm s^{-1}, which indicates a reduced electron transfer process inside the GF. Interestingly, the time constant τ, as defined by Eq. (2), for the GF electrode was higher than that for the GF–$nTiO_2$ electrode (Table 1), indicating a fast reaction for redox conversion. However, the immunoelectrode BSA/anti-*ErbB2*/GF–$nTiO_2$ had a high τ compared to those of the other electrodes (GF, GF-$nTiO_2$, anti-*ErbB2*/GF, and anti-*ErbB2*/GF–$nTiO_2$), presumably because of the slow diffusion of $[Fe(CN)_6]^{3-/4-}$ ions at the protein layer/solution interface of the electrode (Table 1). The surface coverage of anti-*ErbB2* and BSA can be estimated using the relationship $\vartheta = 1 - R_{ct(ele)}/R_{ct(ele+bio)}$, where ϑ is the fraction of the occupied binding sites and $R_{ct(ele)}$ and $R_{ct(ele+bio)}$ are the charge transfer resistances of the electrode before and after immobilizing biomolecules are present, respectively.[43] The ϑ of the GF-based immunoelectrode with and without $nTiO_2$ was 70.1% and 34.2%, respectively. Incorporation of $nTiO_2$ into the GF may be responsible for the higher coverage of anti-*ErbB2* on the GF electrode surface. The BSA/anti-*ErbB2*/GF–$nTiO_2$ immunoelectrode had the maximum ϑ

of 80.4% after BSA immobilization. The higher k_s of the BSA/anti-*ErbB2*/GF–nTiO_2 electrode (3.6 μcm/s) compared to that of other reported electrodes such as BSA/anti-*ErbB2*/ZnO (1.11 μcm/s)[11] and enzyme/TiO_2–CH (0.17 μcm/s)[43] indicates higher electron transfer kinetics of the immunoelectrode used in this sensor.

Table 1. Charge transfer resistance (R_{ct}), double-layer capacitance (C_{dl}), HET rate constant (k_s), time constant (τ), and surface coverage percentage (ϑ) of the fabricated electrodes.

Electrodes	R_{ct} (kΩ)	C_{dl} (μF)	k_s (cm s^{-1})	τ (μs)	ϑ
GF	29.8±0.2	21.5±0.07	18.6±0.1 × 10^{-6}	0.64±0.007	NA
anti-*ErbB2*/GF	45.3±0.1	11.03±0.4	12.2±0.01 × 10^{-6}	0.49±0.008	34.2±0.3%
GF–nTiO_2	86.7±0.2	4.2±0.09	6.4±0.09 × 10^{-6}	0.36±0.004	NA
anti-*ErbB2*/GF–nTiO_2	99.9±0.7	3.9±0.03	5.5±0.03 × 10^{-6}	0.38±0.001	70.1%
BSA/anti-*ErbB2*/GF–nTiO_2	152.6±1.2	3.2±0.01	3.6±0.05 × 10^{-6}	0.48±0.003	80.4±0.7%

Fig. 5b shows the DPV signals at the sensors integrated with the different fabricated electrodes. Due to the higher overall conductivity of the GF, the peak current of DPV for the GF electrode (77.5 μA) was more than three times that for the GF–nTiO_2 electrode (25 μA) and was also higher than that for the anti-ErbB2/GF electrode (63.4 μA). The nTiO_2 on the GF surface reduced the electron transfer rate, as was evident by the smaller k_s obtained in the EIS studies, thus resulting in the lower electrochemical current. Furthermore, the peak current decreased with the incorporation of anti-EbrB2 (21.7 μA) and BSA molecules (18.5 μA) onto the GF–nTiO_2 electrode. This is attributed to the presence of functional groups such as –COOH, C–OH, and N–C=O at the anti-EbrB2- and BSA-immobilized GF–nTiO_2 immunoelectrodes. The reduction of the current is indicative of the immobilization caused by proteins on the surface of GF–nTiO_2.

We have carried out the experiments to investigate DPV responses of our immunosensor under different conditions, including temperature, pH of PBS solution, and concentration of antibody for immobilization. First, to optimize temperature, the microfluidic sensor was tested

under different temperatures using a hotplate. Fig. S4a in Supporting Information presents the DPV responses of the sensor to 0.1 µM concentration of ErbB2 antigen at different temperatures from 20 ºC to 45 ºC. This sensor provided a maximum peak current at 30 ºC. Therefore, all sensing measurements were conducted at 30 ºC. Second, Fig. S4b shows the influence of pH values for the PBS solution on DPV responses of the sensor. Similarly, 0.1 µM concentration of ErbB2 antigen was used in this experiment. Since the maximum peak current was found at pH 7.4 of PBS solution, we performed all sensing measurements at pH 7.4. In addition, we optimized the concentration of anti-ErbB2 used for immobilization. Fig. S4c shows the DVP responses of the sensor functionalized with different anti-ErbB2 concentrations when responding to 0.1 µM concentration of ErbB2. The result shows that the DPV peak current decreased with increasing concentration of antibody molecules. This may perhaps be a consequence of loading more antibody molecules on the sensor surface that allowed capturing more ErbB2 antigen molecules, resulting in a decreased current. When the concentration of antibody solution went beyond 0.24 µM, the peak current was found to saturate. We thus chose 0.24 µM concentration of antibody for immobilization.

To investigate the redox property of the sensor with the BSA/anti-*ErbB2*/GF–nTiO_2 electrode, we conducted cyclic voltammetry (CV) studies at different scan rates (Fig. S5a, Supporting Information). This sensor exhibited well-defined oxidation and reduction properties of the ferro/ferri cyanide mediator used. By increasing the scanning rate from 20 to 500 mV/s, the oxidation and reduction currents increased and decreased, respectively (Fig. S5b), and the oxidation and reduction peak potentials shifted linearly in the positive and negative potential directions, respectively (Fig. S5c). This indicates that the diffusion is surface-controlled and the process is quasi-reversible. The linear equations, slope, regression coefficients, and intercept values for the anodic and cathodic peak currents and the anodic and cathodic potentials are

given in the inset of Figs. S5a and S5b, respectively. The diffusion coefficient (*D*) of redox species $[Fe(CN)_6]^{3-/4-}$ for the fabricated electrodes can be obtained using the Randles–Sevcik equation[52]: i_p (peak current) = 269,000 × $n^{3/2}AD^{1/2}C\,v^{1/2}$, where *n* is the number of electrons transferred in the redox reaction (here, *n* = 1), *A* is the area of the electrode (cm^2), *D* is the diffusion coefficient (cm^2/s), *C* is the surface concentration (mol/cm^2), and *v* is the scanning rate (mV/s). The value of *D* was found to be 15.6, 1.14, 0.636, and 0.207 μ cm^2/s for the GF, GF–$nTiO_2$, anti-*ErbB2*/GF–$nTiO_2$, and BSA/anti-*ErbB2*/GF–$nTiO_2$ electrodes, respectively. The incorporation of $nTiO_2$ into the GF scaffolds resulted in a low diffusion coefficient compared to the GF electrode alone because of the opposite charges between $nTiO_2$ and $[Fe(CN)_6]^{3-/4-}$. The BSA/anti-*ErbB2*/GF–$nTiO_2$ electrode had a *D* value comparable to those of electrodes of other materials, such as ZnS–rGO (6.3 μ cm^2/s)[53] and CysCdS–Au (7.45 μ cm^2/s).[54]

3.4 Detection of Cancer Biomarker. The microfluidic sensor was tested on how well it detected the breast cancer antigen *ErbB2* using the DPV and EIS methods. The concentration of *ErbB2* was varied from 1 ×10^{-15} to 1 ×10^{-7} M or 1.0 fM to 0.1 μM. Fig. 6a shows the DPV for different *ErbB2* concentrations from 1.0 fM to 0.1 μM in the voltage range of 0.3–0.9 V. The sensing potential in the DPV experiments was 0.42 V, at which the maximum peak current occurred. The sensor calibration plot in Fig. 6b shows that the DPV peak current was inversely proportional to the logarithmic concentration of *ErbB2*. The insulating property of the immunocomplex layer formed on the sensor surface barricaded the generated electrons, resulting in a lower current. As the number of *ErbB2* molecules bound to the sensor surface increased, the thickness of the insulating layer increased, thus reducing the voltammetric output current. Fig. 6b shows that the sensitivity of 0.585 μA μM^{-1} was obtained when the sensor was exposed to a wide detection range (1.0 fM to 0.1 μM). Thus, the sensor, in conjunction with the DPV measurement method, offered higher sensitivity (0.585 μA μM^{-1}) in the detection of *ErbB2* molecules than another sensor that also uses DPV but has ZnO nanowire as electrode material[55] (Table 2).

However, the sensitivity of our sensor was lower than those of other sensors that use gold nanoparticles[56] and graphene nanosheets (Table 2).[57]

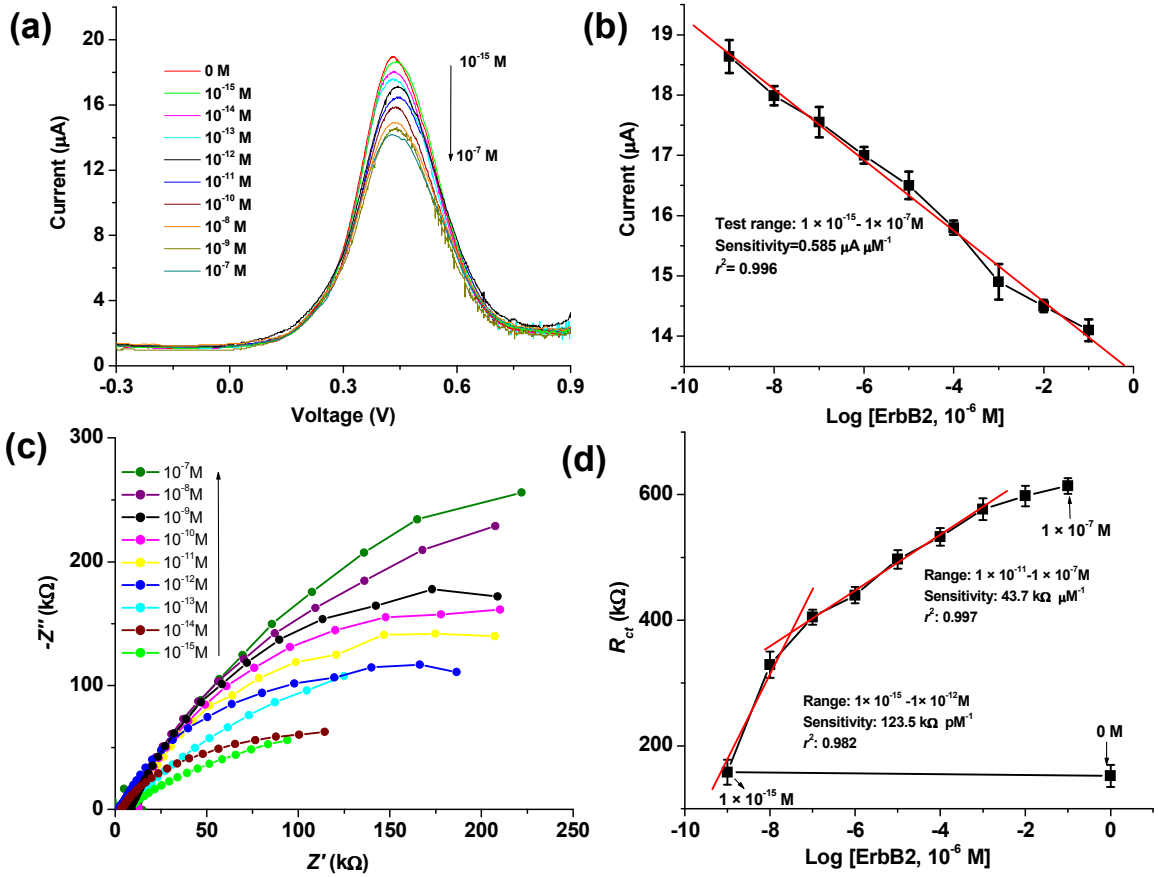

Fig. 6 (a) DPV response curves of the microfluidic immunosensor in detecting different *ErbB2* concentrations. (b) Response calibration plot of the peak DPV current as a function of *ErbB2* concentration. (c) Nyquist plots of the microfluidic immunosensor with the BSA/anti-*ErbB2*/GF–nTiO_2 electrode for detecting *ErbB2* at different concentrations. (d) Response calibration plot of R_{ct} as a function of [*ErbB2*]. The linear test range of [*ErbB2*] was 1.0 fM to 0.1 μM. In both the DPV and EIS measurements, [*ErbB2*] ranged from 1.0 fM to 0.1 μM in PBS solution of pH 7.4 and incubation time of 5 min. In each experiment, *ErbB2* was exposed to the sensor and then washed with PBS solution. The error bars were derived from the relative standard deviation of three measurements at each concentration.

A control experiment for the sensor was carried out with (5 mM) and without $Fe(CN)_6^{3-/4-}$. Without $Fe(CN)_6^{3-/4-}$, the impedance response exhibited a nearly straight line with a high R_{ct} value of 1.5 MΩ. However, after adding 5 mM concentration of $Fe(CN)_6^{3-/4-}$, the sensor provided a semicircle Nyquist plot

with a reduced R_{ct} value of 202 kΩ owing to the presence of $Fe(CN)_6^{3-/4-}$ mediator. Fig. 6c shows the Nyquist plots obtained from the EIS measurements at different concentrations of *ErbB2* antigen. Table S2 shows the EIS parameters of R_{ct}, R_s and C_{dl} obtained at different concentrations of target ErbB2 antigen. These parameters were extracted from the simulated EIS curves and one example of how the parameters were extracted from the Nyquist plot is given in Fig. S7. Fig. 6d shows that R_{ct} increased with increasing concentration of *ErbB2*. This occurred essentially because of the interaction between anti-*ErbB2* and *ErbB2* at the binding sites, i.e., paratope for antibody and epitope for antigen, on the sensor interface, which formed the immunocomplex seen in Fig. 2. The higher R_{ct} indicates that the presence of the insulating layer of *ErbB2* on the anti-*ErbB2*/GF–nTiO_2 electrode impeded the penetration of the redox species, as indicated by the larger diameter of the semicircle of the Nyquist plot (Fig. 6c) and the lower k_s value (Table 1). The negatively charged *ErbB2* on the sensor surface repelled the generated electrons, resulting in a higher impedance signal.[58] The response of R_{ct} for this sensor showed two linear regions of concentration of *ErbB2*, i.e., from 1×10^{-15} to 1×10^{-12} M (or 1.0 fM to 1.0 pM) and from 1×10^{-11} to 1×10^{-7} M (or 10 pM to 0.1 μM). Table 2 compares our sensor with other sensors reported in literature with respect to the performance of detecting target cancer biomarkers. Our sensor exhibited competitive sensitivity (123.5 kΩ pM^{-1} for 1.0 fM to 0.1 pM, and 43.4 kΩ μM^{-1} for 0.1 pM to 0.1 μM) in the detection of *ErbB2* compared to other sensors with cysteamine-gold nanoparticles (3.83 kΩ pM^{-1} for 7.4 fM to 7.4 nM)[59] and functionalized ZnO nanofibers (7.76 kΩ μM^{-1} for 1.0 fM to 0.1 μM).[11] The higher sensitivity of this microfluidic device is due to the porous and large surface feature of nTiO_2 coated three-dimensional GF electrode that allow more loading of anti-ErbB2 receptors for their interactions with specific ErbB2 antigens. Furthermore, the EIS and DPV measurement results indicate that our sensor, in terms of sensitivity, worked better with the EIS method than the DPV method for the detection of *ErbB2*.

Table 2 also shows that other breast cancer biomarker sensors with CdTe–CdS quantum dots,[60] optofluidic ring resonators,[7] Au nanoparticles,[56] and GO–SiO_2[23] had detection ranges of 25 fM–25 nM, 189.5 pM–1.46 nM, 1.4 pM–145.7 pM, and 1 pM–1 µM, respectively. The available functional groups of the carbon-doped $nTiO_2$ and the large surface area of the $nTiO_2$–GF allowed more antibody molecules to be loaded, resulting in the detection of femtomoles of antibodies and over a wider biomarker concentration range from 1.0 fM to 0.1 µM.

Table 2. Comparison of the performance of our device with that of other electrochemical sensors

Bioelectrodes	Measurement methods	Biomarkers	Sensitivity	Detection range
Opto-fluidic ring resonator[7]	Whispering gallery mode	HER2	30 nm/RIU	189.5 pM–1.46 nM
CdTe-CdS quantum dots[60]	Fluorescence	Carcinoma embryonic antigen	NA	25 fM–25 nM
Zinc oxide nanowires[55]	Pulse voltammetry	BRCA1	6.36 nA μM^{-1}	10.0–100.0 µM
Graphene nanosheets[57]	Pulse voltammetry	Carcinoembryonic antigen	0.1 µA pM^{-1}	2.7–333.3 pM
AuNPs[56]	Pulse voltammetry	HER2	0.076 µA pM^{-1}	1.4–145.7 pM
GF-$nTiO_2$ *(this work)*	Pulse voltammetry	ErbB2	0.585 µA μM^{-1}	1.0 fM–0.1 µM
Reduced graphene oxide-SiO_2 nanoparticles[23]	Impedance	HER2	NA	1.0 pM–1.0 µM
Functionalized ZnO nanofibers[11]	Impedance	ErbB2	7.76 kΩ μM^{-1}	1.0 fM–0.1 µM
Cysteamine-AuNPs[59]	Impedance	EGFR	3.83 kΩ pM^{-1}	7.4 fM–7.4 nM
GF-$nTiO_2$ (*this work*)	Impedance	ErbB2	123.5 kΩ pM^{-1}	1.0 fM–0.1 pM
			43.7 kΩ μM^{-1}	0.1 pM–0.1 µM

The antibody–antigen binding kinetics of the $nTiO_2$–GF composite-based electrode were studied using the Hill plot.[61] The association and dissociation behavior of an antibody–antigen complex on the surface of an immunoelectrode can be expressed by Eq. (4):

$$n\mathrm{Ag}' + \mathrm{Ab} \underset{K_\mathrm{d}}{\overset{K_\mathrm{a}}{\Leftrightarrow}} \mathrm{Ag}'_n\mathrm{Ab} \quad (4)$$

where K_a and K_d are the association and dissociation constants, respectively, Ag′ represents *ErbB2* antigen in solution, Ab denotes the immobilized anti-*ErbB2* on the sensor surface, Ag'_nAb

is the antigen–antibody complex, and *n* represents the Hill coefficient or the degree of binding. The dissociation constant for the interaction between *ErbB2* and anti-*ErbB2* is $K_d = 1/K_a = [Ag']^n[Ab]/[Ag'_nAb]$. A low K_d value indicates strong binding between *ErbB2* antigen and anti-*ErbB2*. The Hill coefficient is equivalent to the slope of the Hill plot. Therefore, K_a can be derived from the ordinate intercept of the Hill plot, based on Eq. (5), and its reciprocal is K_d.

$$\log \frac{Y}{1-Y} = \log \frac{1}{K_d} + n\log[ErbB2] \quad (5)$$

where $Y = \Delta R_{ct}/\Delta R_{ct(max)}$ and ΔR_{ct} and $\Delta R_{ct(max)}$ denote the change and the maximum change in charge transfer resistance, respectively. Based on the Hill plot for *ErbB2* (Fig. S8, Supporting Information), the values of K_d, K_a, and *n* for our sensor were 2.32×10^{-3} M, 0.43×10^3 M, and 0.24, respectively. An $n < 1$ indicates negative cooperativity of the immunocomplex between *ErbB2* and anti-*ErbB2* on the sensor surface and a decrease in the affinity of anti-*ErbB2*/GF–nTiO_2 with other molecules. The low K_d of this sensor may be responsible for the higher affinity of the anti-*ErbB2* toward the *ErbB2* antigen.

Figs. 7a and 7b show the transient response of the sensor in the presence of *ErbB2* using the EIS method. When the sensor was exposed to a [*ErbB2*] of 1 nM, the real-axis impedance was saturated after 198 s in the EIS method. The longer detection time of the EIS method may be due to the need to measure the impedance at multiple frequencies until the impedance signal is saturated. We also monitored the transient amperometric current for the detection of 1 nM of *ErbB2*. The current was saturated within about 1 s at 0.3 V and –0.3 V.

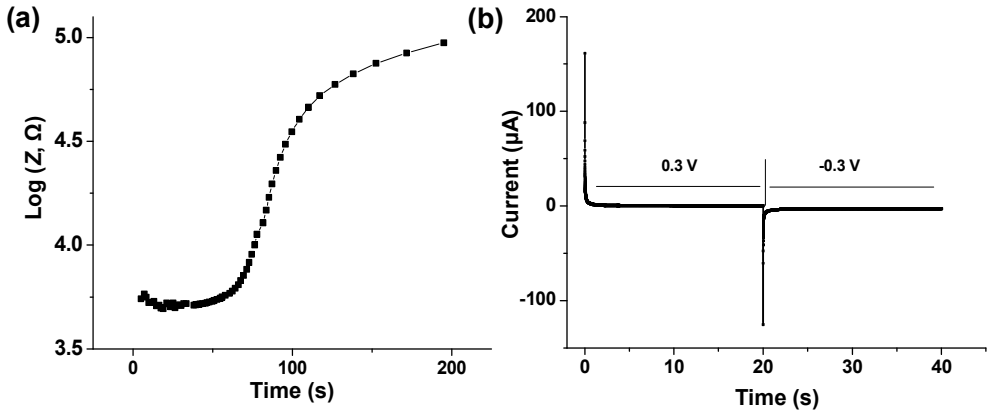

Fig. 7. Transient response of the microfluidic immunosensor for breast cancer *ErbB2* (1 nM) monitoring: (a) impedance versus detection time using the EIS method and (b) amperometric current versus detection time.

To test the selectivity of the sensor, we exposed it to two interfering nonspecific antigens, i.e., *ErbB3* and *ErbB4*, both in the *ErbB* receptor tyrosine kinase family. The DPV method was used to measure the response of the sensor to the presence of the interfering antigens (Figs. 8a and 8b). *ErbB2*, *ErbB3*, and *ErbB4* each had a concentration of 1 nM. Without the *ErbB2* antigen, the microfluidic sensor had a low relative standard deviation (RSD) of ±2.5% from the immunoelectrode (BSA/anti-*ErbB2*/GF–nTiO_2) signal (Fig. 8b). When 1 nM of specific *ErbB2* antigen was added to the solution containing nonspecific *ErbB3*, *ErbB4*, and *ErbB3*+*ErbB4* antigens, the peak current of the sensor did not significantly change, as evidenced by the low RSD (±0.5%). This result demonstrates the good selectivity of the sensor for detecting *ErbB2* overexpressed by breast cancer cells. The high selectivity is due to the specific anti-*ErbB2* binding sites on the sensor surface and the strong interactions with *ErbB2*. Within 42 days of putting the immunosensor through a stability test, we observed a low RSD of ±1.0% when the sensor was stored in 4 °C (Fig. 8c) because of the strong covalent bond of anti-*ErbB2* to the GF–nTiO_2 matrix. Fig. 8d shows the reproducibility of the fabricated device in which five immunoelectrodes were tested, keeping the area of the electrode constant (0.096 cm^2) using

both DPV and EIS methods. The DPV measurement result shows that the deviation of these sensors was ±2.5%, indicating reasonable reproducibility. In addition, the EIS measurement result shows a deviation of ±5 % for the value of R_{ct} as shown in Fig. S9a. To explore the extreme case of detecting 10^{-15} M (1.0 fM), we also conducted four repeated measurements using one of the sensors. The sensor provided a low deviation of ±2.95% for the value of R_{ct} from the initial sensor response. This result indicates that the sensor was reproducible even at 1.0 fM of ErbB2.

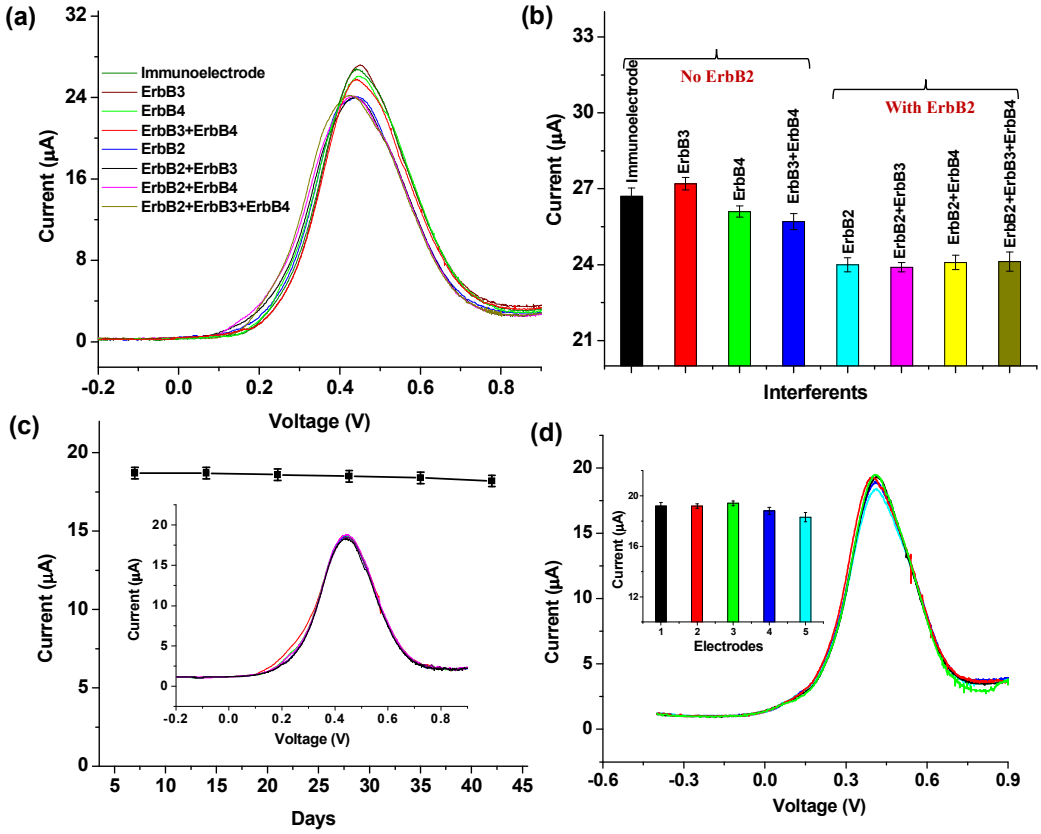

Fig. 8. (a) DPV response curves of the selectivity test of our sensor in the presence of *ErbB3* and *ErbB4* antigens. (b) Histogram showing the peak current of the sensor in the presence of different interferents. (c) Stability of the sensor was tested for various numbers of days within a 7-day interval. Inset shows the DPV of the fabricated sensor obtained at different time points within 42 days. (d) DPV responses of the reproducibility test using five different sensors. Inset histogram shows the peak current of the five electrodes. *ErbB2* had a concentration of 1×10^{-12} M or 1 pM for the stability and reproducibility tests.

4. CONCLUSION

We presented a selective, reproducible, and stable microfluidic immunosensor for the detection of breast cancer molecules via antigen-antibody interactions. The sensor utilized a new immunoelectrode made of hierarchical GF modified with electrospun carbon-doped $nTiO_2$ as the electrochemical working electrode. The excellent electrochemical properties of the GF–$nTiO_2$ matrix of the device allow for sensitive detection of the *ErbB2* antigen, at minute (1.0 fM) to higher (0.1 μM) concentrations, overexpressed in breast cancer cells. The sensor interfaced with two electrochemical measurement methods, impedance and pulse voltammetry, used to detect the *ErbB2* antigen. With the impedance method (EIS), the higher sensitivity of the device was responsible for the impedimetric property of the $nTiO_2$ coated on the GF scaffolds. The functional groups at the GF–$nTiO_2$ composite interface with anti-*ErbB2* and their shape and size were confirmed by XPS, SEM, and TEM. The DPV method also found that the sensor had reasonable sensitivity to *ErbB2* within a wide concentration range. Our sensor is highly selective for *ErbB2* in the presence of interfering *ErbB3* and *ErbB4* antigens. Our sensor can be modified flexibly for the addition of a multifunctional chip to realize multiplexed detection of multiple biomarkers such as *ErbB1*, *ErbB3*, and *ErbB4*. Efforts will be made to investigate using modified devices to test serum or cell lysate samples.

Supporting Information

Raman and X-ray photoelectron spectroscopy (XPS) spectra, a table summarizing binding energies, full width half maximum (FWHM) and atomic ratio, temperature, pH and optimization of antibody concentration using DPV, scan rate studies in cyclic voltammetry (CV) measurements, control studies using EIS, simulation of Nyquist plot, another table summarizing EIS parameters, Hill plot for

kinetic binding studies, and reproducibility studies. This material is available free of charge via the Internet at http://pubs.acs.org.

Notes

The authors declare no competing financial interest.

Author Information

Corresponding Author

*Liang Dong; E-mail: ldong@iastate.edu; Phone: +1-515-294-0388.

Acknowledgements

This work was supported in part by the National Science Foundation under grants ECCS-1102354 and DBI-1353819, and the Iowa State University's Plant Sciences Institute. The authors also thank Dr. Warren Straszheim for SEM measurement, and Dr. Daping Jing for XPS measurement.

References

1. Wang, J., Electrochemical Biosensors: Towards Point-of-Care Cancer Diagnostics. *Biosens. Bioelectron.* **2006**, *21*, 1887-1892.
2. Yetisen, A. K.; Akram M. S.; Lowe, C. R., Paper-Based Microfluidic Point-of-Care Diagnostic Devices. *Lab on a Chip* **2013**, *13*, 2210-2251.
3. Tothill, I. E., Biosensors for Cancer Markers Diagnosis. *Sem. Cell. Dev. Biol.*, **2009**, *20*, 55-62.
4. Li, H.; He, J.; Li S.; Turner, A. P. F., Electrochemical Immunosensor with N-Doped Graphene-Modified Electrode for Label-Free Detection of the Breast Cancer Biomarker CA 15-3. *Biosens. Bioelectron.* **2013**, *43*, 25-29.
5. Roskoski, Jr. R., The ErbB/HER Family of Protein-Tyrosine Kinases and Cancer. *Pharmacol. Res.* **2014**, *79*, 34-74.

6. Moulder, S. L.; Yakes, F. M.; Muthuswamy, S. K.; Bianco, R.; Simpson, J. F.; Arteaga, C. L., Epidermal Growth Factor Receptor (HER1) Tyrosine Kinase Inhibitor ZD1839 (Iressa) Inhibits HER2/neu (erbB2)-Overexpressing Breast Cancer Cells in Vitro and in Vivo. *Cancer Res.* **2001**, *61*, 8887-8895.
7. Gohring, J. T.; Dale P. S.; Fan, X., Detection of HER2 Breast Cancer Biomarker using the Opto-Fluidic Ring Resonator Biosensor. *Sens. Actuators, B* **2010**, *146*, 226-230.
8. Yu, D.; Hung, M. C., Breast Cancer Chemosensitivity, *Springer New York*, Texas, USA, 2009.
9. Yarden, Y.; Sliwkowski, M. X.; Untangling the ErbB Signalling Network. *Nat. Rev. Mol. Cell. Biol.* **2001**, *2*, 127-137.
10. Agus, D. B.; Akita, R. W.; Fox, W. D.; Lewis, G. D.; Higgins, B.; Pisacane, P. I.; Lofgren, J. A.; Tindell, C.; Evans, D. P.; Maiese, K.; Scher, H. I.; Sliwkowski, M. X., Targeting Ligand-Activated ErbB2 Signaling Inhibits Breast and Prostate Tumor Growth. *Cancer Cell* **2002**, *2*, 127-137.
11. Ali, Md. A.; Mondal, K.; Singh, C.; Malhotra, B. D.; Sharma, A., Anti-Epidermal Growth Factor Receptor Conjugated Mesoporous Zinc Oxide Nanofibers for Breast Cancer Diagnostics. *Nanoscale* **2015**, *7*, 7234-7245.
12. Findlay, J. W. A.; Smith, W. C.; Lee, J. W.; Nordblom, G. D.; Das, I.; DeSilva, B. S.; Khan, M. N.; Bowsher, R. R., Validation of Immunoassays for Bioanalysis: A Pharmaceutical Industry Perspective. *J. Pharm. Biomed. Anal.* **2000**, *21*, 1249-1273.
13. Kerns, B. J.; Pence, J. C.; Huper, G.; Kinney, R. B.; Iglehart, J. D., c-erbB-2 Expression In Breast Cancer Detected by Immunoblotting and Immunohistochemistry. *J. Histochem. Cytochem.* **1990**, *38*, 1823-1830.
14. Vessella, R. L.; Noteboom, J.; Lange, P. H., Evaluation of the Abbott lMx® Automated Immunoassay of Prostate-Specific Antigen. *Clin. Chem.* **1992**, *38*, 2044-2054.
15. Butch, A. W.; Crary, D.; Yee, M., Analytical Performance of the Roche Total and Free PSA Assays on the Elecsys 2010 Immunoanalyzer. *Clin. Biochem.* **2002**, *35*, 143-145.
16. Woodrum, D. L.; French, C. M.; Hill, T. M.; Roman, S. J.; Slatore, H. L.; Shaffer, J. L.; York, L. G.; Eure, K. L.; Loveland, K. G.; Gasior, G. H.; Southwick, P. C.; Shamel, L. B., Analytical Performance of the Tandem®-R Free PSA Immunoassay Measuring Free Prostate-Specific Antigen. *Clin. Chem.* **1997**, *43*, 1203-1208.
17. Yu, X.; Munge, B.; Patel, V.; Jensen, G.; Bhirde, A.; Gong, J. D.; Kim, S. N.; Gillespie, J.; Gutkind, J. S.; Papadimitrakopoulos, F.; Rusling, J. F., Carbon Nanotube Amplification

Strategies for Highly Sensitive Immunodetection of Cancer Biomarkers. *J. Am. Chem. Soc.* **2006**, *128*, 11199-11205.

18. Krishnan, S.; Mani, V.; Wasalathanthri, D.; Kumar, C. V.; Rusling, J. F., Attomolar Detection of a Cancer Biomarker Protein in Serum by Surface Plasmon Resonance Using Superparamagnetic Particle Labels *Angew. Chem. Int. Ed.* **2010**, *50*, 1175-1178.
19. Chan, L. L.; Gosangari, S. L.; Watkin, K. L.; Cunningham, B. T., A Label-Free Photonic Crystal Biosensor Imaging Method for Detection of Cancer Cell Cytotoxicity and Proliferation. *Apoptosis* **2007**, *12*, 1061-1068.
20. Wee, K. W.; Kang, G. Y.; Park, J.; Kang, J. Y.; Yoon, D. S.; Park, J. H.; Kim, T. S., Novel Electrical Detection of Label-Free Disease Marker Proteins using Piezoresistive Self-Sensing Micro-Cantilevers. *Biosens. Bioelectron.* **2005**, *20*, 1932-1938.
21. Wu, X.; Liu, H.; Liu, J.; Haley, K. N.; Treadway, J. A.; Larson, J. P.; Ge, N.; Peale, F.; Bruchez, M. P.; Immunofluorescent Labeling of Cancer Marker Her2 and Other Cellular Targets with Semiconductor Quantum Dots. *Nat. Biotechnol.* **2003**, *21*, 41-46.
22. Ho, S.-L.; Xu, D.; Wong, M. S.; Li, H.-W., Direct and Multiplex Quantification of Protein Biomarkers in Serum Samples using an Immunomagnetic Platform. *Chem. Sci.* **2016**, *7*, 2695-2700.
23. Myung, S.; Solanki, A.; Kim, C.; Park, J.; Kim, K. S.; Lee, K.-B., Graphene-Encapsulated Nanoparticle-Based Biosensor for the Selective Detection of Cancer Biomarkers. *Adv. Mater.* **2011**, *23*, 2221-2225.
24. Mani, V.; Chikkaveeraiah, B. V.; Patel, V.; Gutkind, J. S.; Rusling, J. F., Ultrasensitive Immunosensor for Cancer Biomarker Proteins Using Gold Nanoparticle Film Electrodes and Multienzyme-Particle Amplification. *ACS Nano* **2009**, *3*, 585-594.
25. Wang, J.; Xu, D.; Polsky, R., Magnetically-Induced Solid-State Electrochemical Detection of DNA Hybridization. *J. Am. Chem. Soc.* **2002**, *124*, 4208-4209.
26. Gao, X.; Zhang, Y.; Chen, H.; Chen, Z.; Lin, X., Amperometric Immunosensor for Carcinoembryonic Antigen Detection with Carbon Nanotube-Based Film Decorated with Gold Nanoclusters. *Anal. Biochem.* **2011**, *414*, 70-76.
27. Lu, C.-H.; Yang, H.-H.; Zhu, C.-L.; Chen, X., Chen, G.-N., A Graphene Platform for Sensing Biomolecules. *Angew. Chem.* **2009**, *121*, 4879-4881.
28. Geim, A. K., Graphene: Status and Prospects. *Science* **2009**, *324*, 1530-1534.

29. Ali, Md. A.; Singh, C.; Mondal, K.; Srivastava, S.; Sharma, A.; Malhotra, B. D., Mesoporous Few-Layer Graphene Platform for Affinity Biosensing Application. *ACS Appl. Mater. Interfaces* **2016**, *8*, 7646-7656.

30. Wu, Z.-S.; Sun, Y.; Tan, Y.-Z.; Yang, S.; Feng, X.; Müllen, K., Three-Dimensional Graphene-Based Macro- and Mesoporous Frameworks for High-Performance Electrochemical Capacitive Energy Storage. *J. Am. Chem. Soc.* **2012**, *134*, 19532-19535.

31. Chen, Z.; Ren, W.; Gao, L.; Liu, B.; Pei, S.; Cheng, H.-M., Three-Dimensional Flexible and Conductive Interconnected Graphene Networks Grown by Chemical Vapour Deposition *Nat. Mater.* **2011**, *10*, 424-428.

32. Dong, X.-C.; Xu, H.; Wang, X.-W.; Huang, Y.-X.; Chan-Park, M. B.; Zhang, H.; Wang, L.-H.; Huang, W.; Chen, P., 3D GrapheneCobalt Oxide Electrode for High-Performance Supercapacitor and Enzymeless Glucose Detection. *ACS Nano* **2012**, *6*, 3206-3213.

33. Dong, X.; Cao, Y.; Wang, J.; Chan-Park, M. B.; Wang, L.; Huang, W.; Chen, P., Hybrid Structure of Zinc Oxide Nanorods and Three Dimensional Graphene Foam for Supercapacitor and Electrochemical Sensor Applications. *RSC Adv.* **2012**, *2*, 4364-4369.

34. Shao, D.; Gao, J.; Xin, G.; Wang, Y.; Li, L.; Shi, J.; Lian, J.; Koratkar, N.; Sawyer, S., Cl-Doped ZnO Nanowire Arrays on 3D Graphene Foam with Highly Efficient Field Emission and Photocatalytic Properties. *Small* **2015**, *11*, 4785-4792.

35. Yue, H. Y.; Huang, S.; Chang, J.; Heo, C.; Yao, F.; Adhikari, S.; Gunes, F.; Liu, L. C.; Lee, T. H.; Oh, E. S.; Li, B.; Zhang, J. J.; Huy, T. Q.; Luan, N. V.; Lee, Y. H., ZnO Nanowire Arrays on 3D Hierachical Graphene Foam: Biomarker Detection of Parkinson's Disease. *ACS Nano* **2014**, *8*, 1639-1646.

36. Si, P.; Dong, X.-C.; Chen, P.; Kim, D.-H., A Hierarchically Structured Composite of Mn_3O_4/3D Graphene Foam for Flexible Nonenzymatic Biosensors. *J. Mater. Chem. B*, **2013**, *1*, 110-115.

37. Ahmad, M.; Pan, C.; Luo, Z.; Zhu, J., A Single ZnO Nanofiber-Based Highly Sensitive Amperometric Glucose Biosensor. *J. Mater. Chem. C* **2010**, *114*, 9308-9313.

38. Mondal, K.; Ali, Md. A.; Agrawal, V. V.; Malhotra, B. D.; Sharma, A., Highly Sensitive Biofunctionalized Mesoporous Electrospun TiO_2 Nanofiber Based Interface for Biosensing. *ACS Appl. Mater. Interfaces* **2014**, *6*, 2516-2527.

39. Solanki, P. R.; Kaushik, A.; Agrawal, V. V.; Malhotra, B. D., Nanostructured Metal Oxide-Based Biosensors. *NPG Asia Mater*. **2011**, *3*, 17-24.

40. Curreli, M.; Li, C.; Sun, Y.; Lei, B.; Gundersen, M. A.; Thompson, M. E.; Zhou, C., Selective Functionalization of In_2O_3 Nanowire Mat Devices for Biosensing Applications. *J. Am. Chem. Soc.* **2005**, *127*, 6922-6923.

41. Wang, R.; Ruan, C.; Kanayeva, D.; Lassiter, K.; Li, Y., TiO_2 Nanowire Bundle Microelectrode Based Impedance Immunosensor for Rapid and Sensitive Detection of Listeria monocytogenes. *Nano Lett.* **2008**, *8*, 2625-2631.

42. Papageorgiou, A. C.; Beglitis, N. S.; Pang, C. L.; Teobaldi, G.; Cabailh, G.; Chen, Q.; Fisher, A. J.; Hofer, W. A.; Thornton, G., Electron Traps and Their Effect on the Surface Chemistry of TiO_2 (110). *Proc. Natl. Acad. Sci. U. S. A.* **2010**, *107*, 2391-2396.

43. Ali, Md. A.; Srivastava, S.; Mondal, K.; Chavhan, P. M.; Agrawal, V. V.; John, R.; Sharma, A.; Malhotra, B. D., A Surface Functionalized Nanoporous Titania Integrated Microfluidic Biochip. *Nanoscale* **2014**, *6*, 13958-13969.

44. Ali, Md. A.; Srivastava, S.; Solanki, P. R.; Agrawal, V. V.; John, R.; Malhotra, B. D., Nanostructured Anatase-Titanium Dioxide Based Platform for Application to Microfluidics Cholesterol Biosensor. *Appl. Phys. Lett.* **2012**, *101*, 084105.

45. Li, D.; Xia, Y., Fabrication of Titania Nanofibers by Electrospinning. *Nano Lett.* **2003**, *3*, 555-560.

46. Mondal, K.; Bhattacharyya, S.; Sharma, A.; Photocatalytic Degradation of Naphthalene by Electrospun Mesoporous Carbon-Doped Anatase TiO_2 Nanofiber Mats. *Ind. Eng. Chem. Res.* **2014**, *53*, 18900-18909.

47. Katiyar, S.; Mondal, K.; Sharma, A., One-Step Sol–Gel Synthesis of Hierarchically Porous, Flow-Through Carbon/Silica Monoliths. *RSC Adv.* **2016**, *6*, 12298-12310.

48. Mondal, K.; Ali, Md. A.; Srivastava, S.; Malhotra, B. D.; Sharma, A., Electrospun Functional Micro/Nanochannels Embedded in Porous Carbon Electrodes for Microfluidic Biosensing. *Sens. Actuators, B.* **2016**, *229*, 82-91.

49. Liu, J.; Zhang, Q.; Yang, J.; Ma, H.; Tade, M. O.; Wang, S.; Liu, J., Facile Synthesis of Carbon-Doped Mesoporous Anatase TiO_2 for the Enhanced Visible-Light Driven Photocatalysis. *Chem. Commun.* **2014**, *50*, 13971-13974.

50. Li, N.; Zhang, Q.; Gao, S.; Song, Q.; Huang, R.; Wang, L.; Liu, L.; Dai, J.; Tang, M.; Cheng, G., Three-Dimensional Graphene Foam as a Biocompatible and Conductive Scaffold for Neural Stem Cells. *Sci. Rep.* **2013**, *3*, 1604.

51. Kaushik, A.; Solanki, P. R.; Kaneto, K.; Kim, C. G.; Ahmad, S.; Malhotra, B. D., Nanostructured Iron Oxide Platform for Impedimetric Cholesterol Detection. *Electroanalysis* **2010**, *22*, 1045-1055.

52. Martin-Yerga, D.; Costa, R. E.; Garcia, A. C., Electrochemical Study and Determination of Electroactive Species with Screen-Printed Electrodes. *J. Chem. Educ.* **2016**, DOI: 10.1021/acs.jchemed.1025b00755.

53. Mishra, S. K.; Srivastava, A. K.; Kumar, D.; Biradar, A. M.; Rajesh, Microstructural and Electrochemical Impedance Characterization of Bio-functionalized Ultrafine ZnS Nanocrystals–Reduced Graphene Oxide Hybrid for Immunosensor Applications. *Nanoscale* **2013**, *5*, 10494-10503.

54. Ali, Md. A., Srivastava, S.; Pandey, M. K.; Agrawal, V. V.; John, R.; Malhotra, B. D., Protein−Conjugated Quantum Dots Interface: Binding Kinetics and Label-Free Lipid Detection. *Anal. Chem.* **2014**, *86*, 1710-1718.

55. Mansor, N. A.; Zain, Z. M.; Hamzah, H. H.; Noorden, M. S. A.; Jaapar, S. S.; Beni, V.; Ibupoto, Z. H., Detection of Breast Cancer 1 (BRCA1) Gene Using an Electrochemical DNA Biosensor Based on Immobilized ZnO Nanowires. *Open J. Appl. Biosens.* **2014**, *3*, 9-17.

56. Zhu, Y.; Chandra, P.; Shim, Y.-B., Ultrasensitive and Selective Electrochemical Diagnosis of Breast Cancer Based on a Hydrazine–Au Nanoparticle–Aptamer Bioconjugate. *Anal. Chem.* **2013**, *85*, 1058-1064.

57. Chen, X.; Jia, X.; Han, J.; Ma, J.; Ma, Z., Electrochemical Immunosensor for Simultaneous Detection of Multiplex Cancer Biomarkers Based on Graphene Nanocomposites. *Biosens. Bioelectron.* **2013**, *50*, 356-361.

58. Feroz, K.; Williams, E.; Riese Ii, D. J., ErbB2 and ErbB3 Do Not Quantitatively Modulate Ligand-Induced ErbB4 Tyrosine Phosphorylation. *Cell. Signalling* **2002**, *14*, 793-798.

59. Elshafey, R.; Tavares, A. C.; Siaj, M.; Zourob, M., Electrochemical Impedance Immunosensor based on Gold Nanoparticles–Protein G for the Detection of Cancer Marker Epidermal Growth Factor Receptor in Human Plasma and Brain Tissue. *Biosens. Bioelectron.* **2013**, *50*, 143-149.

60. Hu, M.; Yan, J.; He, Y.; Lu, H.; Weng, L.; Song, S.; Fan, C.; Wang, L., Ultrasensitive, Multiplexed Detection of Cancer Biomarkers Directly in Serum by Using a Quantum Dot-Based Microfluidic Protein Chip. *ACS Nano* **2010**, *4*, 488-494.

61. Guntupalli, R.; Lakshmanan, R. S.; Johnson, M. L.; Hu, J.; Huang, T.-S.; Barbaree, J. M.; Vodyanoy, V. J.; Chin, B. A., Magnetoelastic Biosensor for the Detection of Salmonella Typhimurium in Food Products. *Sens Instrum. Food Qual. Saf.* **2007**, *1*, 3-10.

Table of Contents